Research Square

Preprints are preliminary reports that have not undergone peer review.
They should not be considered conclusive, used to inform clinical practice,
or referenced by the media as validated information.

EMD–Conv1D–LSTM for P-Wave Picking in High-Speed Rail Earthquake Early Warning

Changwei Yang
Southwest Jiaotong University
Xiaoyang Li
Southwest Jiaotong University
Jing Lian
lianjingxhu@163.com

Xihua University
Baorui Hou
Southwest Jiaotong University
Xinqi Ouyang
Southwest Jiaotong University
Xinyu Liang
Southwest Jiaotong University

Research Article

Keywords: High-speed railway, earthquake early warning, P-wave arrival-time picking, EMD–Conv1D–LSTM, robustness

Posted Date: November 4th, 2026

DOI: https://doi.org/10.21203/rs.3.rs-11298489/v1

License: This work is licensed under a Creative Commons Attribution 4.0 International License.
Read Full License

Additional Declarations: Competing interest reported. The authors declare that they have no known competing financial interests or personal relationships that could have appeared to influence the work reported in this paper.

EMD–Conv1D–LSTM for P-Wave Picking in High-Speed Rail Earthquake Early Warning

Changwei Yang[a,b], Xiaoyang Li[a,b], Jing Lian[c,*], Baorui Hou[a,b], Xinqi Ouyang[a,b], Xinyu Liang[a,b]

[a] *School of Civil Engineering, Southwest Jiaotong University, Chengdu 610031, China*

[b] *MOE Key Laboratory of High-speed Railway Engineering, College of Civil Engineering, Southwest Jiaotong University, Chengdu 610031, China*

[c] *School of Architecture and Civil Engineering, Xihua University, Chengdu 610039, China*

**Corresponding author's email address: lianjingxhu@163.com (Jing Lian)*

Abstract: High-speed railways (HSR) are characterized by intense ambient noise, complex vibration interference, and an extremely short early-warning time window, which jointly impose stringent requirements on seismic phase-picking algorithms. To meet the engineering demand of high precision with low false-alarm and missed-detection rates in high-speed railway earthquake early warning (HSR-EEW), this study proposes an automatic P-wave arrival-time picking method based on an empirical mode decomposition–one-dimensional convolution–long short-term memory network (ECL). The overall performance is evaluated in terms of accuracy, error-distribution characteristics, and parameter sensitivity. The results indicate that the proposed ECL algorithm achieves a P-wave picking accuracy of 98.6% with a mean absolute error (MAE) of 0.097 s, outperforming empirical mode decomposition–long short-term memory (EL), empirical mode decomposition–

one-dimensional convolution (EC), short-term average/long-term average (STA/LTA), and Akaike information criterion (AIC) algorithms. The accuracy of traditional algorithms is mainly controlled by amplitude features, whereas AI-based algorithms exhibit better robustness to conventional source parameters. Combining the first-station accuracy analysis, the ECL algorithm achieves high picking accuracy with low error dispersion and strong reliability, providing reliable technical support for automatic P-wave picking in HSR-EEW systems. Combined with the first-station accuracy analysis and field-measured validation, the ECL method demonstrates high P-wave picking accuracy, low error dispersion, and strong robustness to operational interference, providing reliable technical support for automatic P-wave picking in high-speed railway earthquake early warning (HSR-EEW) systems.

Keywords: High-speed railway; earthquake early warning; P-wave arrival-time picking; EMD–Conv1D–LSTM; robustness

1. Introduction

HSR, as a critical infrastructure in modern transportation, is characterized by high operating speeds, dense traffic, and complex line structures. Trains running at high speed are extremely sensitive to seismic hazards. Once an earthquake occurs, if a reliable warning cannot be issued within the very short time window before the arrival of destructive S waves to trigger emergency braking, catastrophic consequences may occur, including derailment, overturning, and damage to trackside facilities [1]–[2]. Therefore, it is essential to develop an efficient and accurate HSR-EEW. In HSR-EEW, P-wave phase identification is the primary step that determines the

timeliness and reliability of early warning [3]. Unlike conventional regional EEW, high-speed rail operates in highly complex electromagnetic and train-noise environments. This requires P-wave identification algorithms to provide faster responses and, under the prerequisite of zero missed detections, to strictly control the false-alarm rate, thereby avoiding substantial operational losses and secondary risks caused by emergency braking triggered by false alerts.

In existing earthquake early-warning systems, P-wave phase identification largely relies on traditional time-domain statistical methods, such as STA/LTA and AIC, and their higher-order variants [4]. STA/LTA highlights abrupt amplitude changes by comparing the energy in short and long time windows and has become a classic benchmark in automatic picking studies [5]; its performance has been further improved by introducing squared envelopes and dynamic-threshold strategies [6]. The AIC method determines phase arrival times according to changes in waveform statistical properties and is often used to refine coarse picking results [7–8]; its identification capability can be further enhanced when combined with multi-band analysis [9]. Baillard et al. [10] proposed an automatic P- and S-phase picking algorithm that combines a characteristic function with eigenvalue decomposition of three-component seismic data. Huang and Wu [11] captured fine P-wave arrival times without preselecting frequency bands, achieving higher picking accuracy and stability than the AIC method. Traditional methods are easy to implement and computationally inexpensive, and have been widely adopted in some seismic networks and engineering applications. However, under the complex noise background along high-speed rail

corridors, non-seismic signals such as train-induced vibrations, trackside wind noise, and surface engineering disturbances become significantly stronger. Traditional methods are sensitive to threshold settings and filtering parameters, leading to false alarms, missed detections, and arrival-time biases [12]. When the signal-to-noise ratio is low, weak P-wave onsets are more difficult to distinguish from transient impulsive noise, leading to a marked decline in identification accuracy and making it difficult to meet the high reliability and stability requirements of high-speed rail earthquake early warning [13].

With the development of artificial intelligence, deep learning, enabled by end-to-end automatic feature extraction, has made notable progress in seismology-related research [14]. Convolutional neural networks (CNNs) and recurrent neural networks (RNNs/LSTMs) have shown excellent performance in tasks such as image recognition, speech processing, and waveform processing [15]. Mousavi et al. [16] utilized the attention mechanism of Transformers to process long seismic sequences, thereby significantly improving the accuracy of P-wave and S-wave picking. Zhu and Beroza [17] directly mapped three-component waveforms to time-probability distributions of P-wave and S-wave phases, and noise using PhaseNet, and achieved high-precision arrival-time picking by identifying probability peaks. Perol et al. [18] proposed a ConvNetQuake model that treats earthquake detection as an image classification problem, enabling the detection and localization of earthquakes from a single waveform. Zhu et al. [19] formulated P-wave identification as a sequence-classification problem and constructed a LSTM network

to model the differences between P waves and background noise, effectively distinguishing P waves from complex background noise. Zhu et al. [20] proposed an end-to-end deep-learning earthquake monitoring method for seismic networks, demonstrating the potential to improve automated monitoring performance through cross-task information sharing. Deep-learning-based phase identification methods can be applied directly to raw or preprocessed seismic waveforms, adaptively learning multi-scale time–frequency features and achieving integrated modeling from feature extraction to decision making. This substantially reduces reliance on handcrafted feature design, yielding higher identification accuracy and robustness under complex noise conditions [21]–[22].

Although deep-learning methods have been introduced into earthquake EEW systems, most existing studies focus on regional seismic networks and still suffer from insufficient identification accuracy and limited adaptability. Dedicated analyses for HSR operating conditions remain lacking. Along HSR corridors, ambient noise and train-induced noise exhibit extremely high energy and show complex mixing and overlap with real seismic P-wave signals in both time and frequency domains. When a relatively simple deep-learning model is used alone to process raw waveforms, it is often difficult to effectively separate such strongly nonlinear and highly non-stationary background noise. As a result, feature extraction is disturbed, which degrades the accuracy and stability of P-wave arrival-time picking.

Based on this, this study, utilizing a HSR-EEW system as its engineering background, proposes a new method for HSR P-wave phase identification using an

ECL architecture. This method applies EMD to the measured vertical-component waveforms recorded at trackside stations, extracting multiple IMFs that represent different frequency-band characteristics and describing the local dynamic evolution of seismic waves across multiple time scales [23–24]. The IMFs, with clear physical meaning, are used as multi-channel inputs, and a Conv1D module is introduced to adaptively extract onset morphology, energy transients, and local time–frequency responses within each mode [25]. An LSTM is then employed to model long-range correlations across modes and along the time sequence, thereby enabling refined identification of P-wave arrival times under complex noise conditions [26]. This approach is not simply a combination of empirical mode decomposition and a deep learning network. Instead, it is designed for the strong non-stationarity and complex interferences in signals along high-speed rail corridors, as well as for the fact that P-wave onset features can be easily masked within short warning windows. Accordingly, it establishes an identification method that integrates signal decomposition, local feature extraction, and temporal-dependency modeling. The results provide technical support for optimizing and engineering the application of automatic P-wave identification algorithms in HSR-EEW systems, and have significant engineering value for enhancing the proactive disaster mitigation capability of HSR under seismic loading.

2. Data and Methods

2.1 Seismic Wave Data and Preprocessing

The seismic waveform data used in this study are three-component

ground-acceleration records from the Japanese K-NET and KiK-net seismic networks. To ensure data consistency, the sampling frequency of all records was unified to 100 Hz. Given that P-wave energy is more concentrated on the vertical component and its initial motion is clearer, the UD component was selected as the primary component for P-wave arrival-time determination and as the model input. The NS and EW components were not used in modelling in this study and were reserved for future research. The P-wave arrival times were labelled using manually picked results as the ground truth. Figure 1 presents the composite acceleration time histories in the EW, NS, and UD directions for a representative event, together with the manually picked P-wave arrival-time annotation.

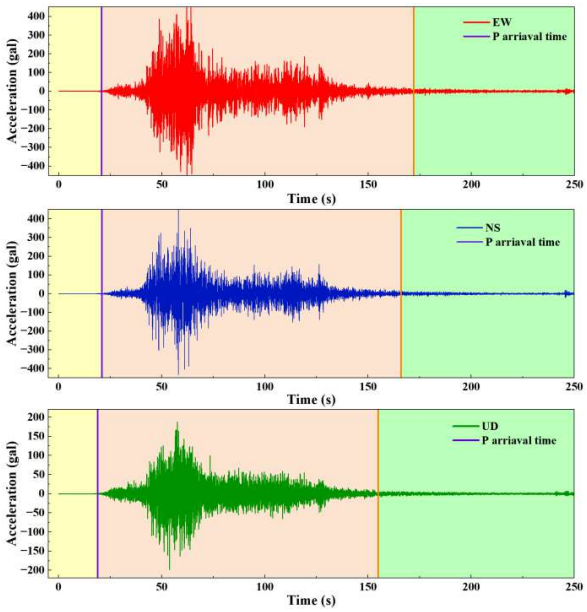


Fig. 1. Phase information in three-component seismic waveforms.

The data preprocessing procedure in this study mainly includes four steps: (1) The raw UD-component records were detrended, de-meaned, and inspected for outliers, and records with evident saturation or severe clipping were excluded. (2) A 0.1–20 Hz band-pass filter was applied to the waveforms, while preserving the main

P-wave frequency-band information as much as possible, to suppress low-frequency baseline drift and high-frequency instrumental noise. (3) Based on the unified sampling rate of 100 Hz, the signals were downsampled, and a fixed-length time window relative to the event onset was extracted to construct sequential samples. (4) The extracted window was ensured to contain the ground-truth P-wave arrival time, while retaining a certain length of pre-arrival noise and post-arrival segments so that the model could learn the complete temporal evolution from background noise to the P-wave onset and then to subsequent strong ground motion. (5) The first three IMFs obtained from EMD were retained as the input channels of the model; for samples with fewer than three IMFs, zero vectors were padded to maintain a consistent input dimension. (6) To eliminate differences in units and amplitude ranges across IMF channels, each IMF component was normalized independently to zero mean and unit standard deviation.

2.2 *EMD–Conv1D–LSTM-Based P-Wave Arrival Picking Model*

To develop a high-precision P-wave arrival-time picking model for HSR-EEW scenarios, this study constructs a joint ECL architecture using EMD, Conv1D, and LSTM, as shown in Fig. 2. A total of 8,514 P-wave samples were selected and split into the training and validation sets at a ratio of 8:2. During training, the Adam optimizer was used with a learning rate of 0.001 and a batch size of 32.

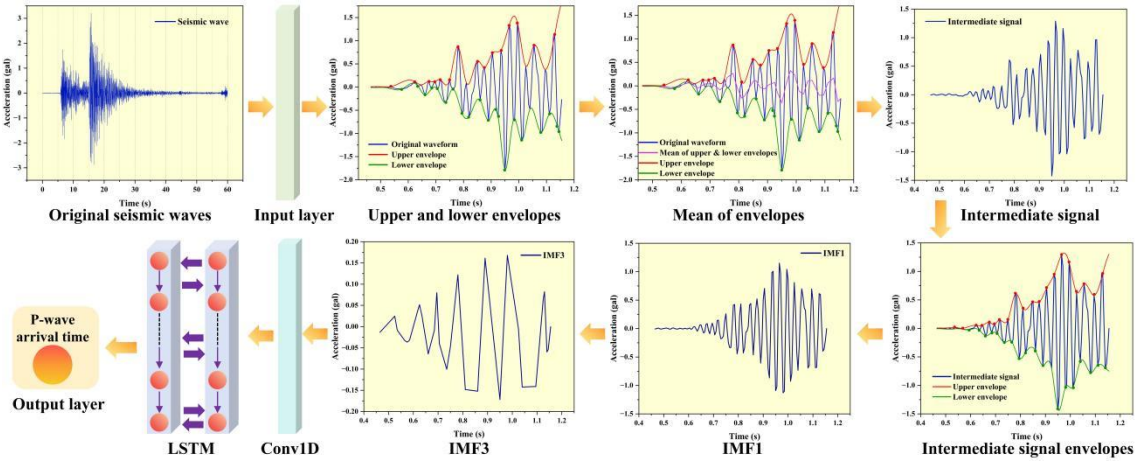


Fig. 2. Joint EMD–Conv1D–LSTM architecture.

Train-induced vibrations and seismic signals show clear overlap in both the time and frequency domains, as illustrated in Fig. 3. The mixed signal contains low-frequency components dominated by ground motion and structural response, as well as high-frequency narrowband components caused by train operation and external disturbances, thereby reducing the distinguishability of the P-wave onset boundary.

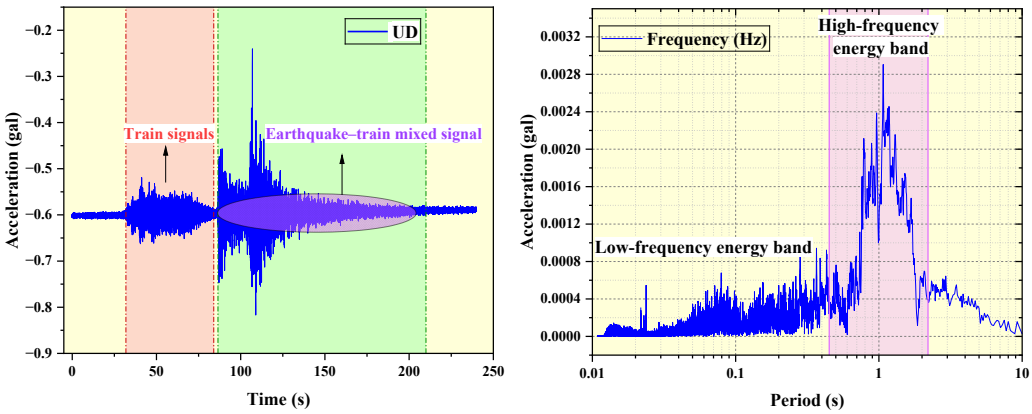


Fig. 3. Schematic diagram of an earthquake–train mixed signal.

In light of this, EMD is applied at the feature-construction stage, and each UD-component waveform is decomposed into several physically meaningful IMFs. During decomposition, the standard deviation threshold is set to 0.05; when the mean

squared difference between two consecutive decomposition results is below this threshold, the component variation is considered stable and the extraction of the current IMF is terminated. The variance-ratio threshold is set to 0.05; when the relative variance falls below this value, the iteration is stopped to control the energy change of the signal before and after sifting. The total energy threshold is set to 0.01; when the residual energy is lower than 1%, the signal is considered sufficiently decomposed. The amplitude-range threshold is set to 0.01; when the amplitude variation range of an IMF is below this value, sifting is terminated. EMD decomposes a non-stationary signal into a series of narrowband components from high to low frequency, enabling high-frequency transients and energy jumps associated with the P-wave onset to be highlighted in specific IMFs. In this study, the first three IMFs are selected as multi-channel inputs. They are stacked along the time steps to form a two-dimensional tensor in time and channels, and each channel is normalized to reduce the influence of amplitude differences across events and stations on training stability.

The network architecture consists of a single 1D convolutional block and a bidirectional LSTM. The Conv1D layer employs 32 convolutional kernels, uses a kernel size of 5 and a padding of 2, to extract local features from the multi-channel IMF sequences and suppress noise. The time-feature sequences compressed by Conv1D are then fed into a two-layer LSTM module with 64 hidden units to model long-term dependencies. Through one-dimensional convolution and pooling operations, Conv1D captures local morphological variations, energy-concentrated

regions, and waveform transient structures near the P-wave onset along the time axis. Using gated mechanisms to retain or discard information selectively, the LSTM effectively represents the temporal evolution from background noise to the P-wave onset and then to subsequent ground motion.

At the output layer, this study adopts a sequence-labelling strategy for arrival-time picking. The LSTM outputs a feature vector at each time step, which is mapped to a one-dimensional scalar through a fully connected layer and then converted by a Sigmoid function into the probability around the P-wave arrival time. Based on the manually picked ground-truth arrival time, a label sequence is constructed by marking several sampling points before and after it as 1 within the window, while assigning 0 to the remaining time steps. Binary cross-entropy loss is used as the optimisation objective, with loss weights applied. Finally, the time step with the maximum probability in the entire probability sequence is selected as the predicted arrival, and the corresponding sample index is converted into time to achieve automatic P-wave arrival-time picking.

The training and validation losses of the ECL model exhibit rapid convergence followed by stable refinement, as shown in Fig. 4. Within the first five epochs, the training loss decreases from 0.37 to approximately 0.06, and the validation loss drops from about 0.18 to about 0.07, indicating that the model quickly learns the main discriminative features at the early stage. From then until the 20th epoch, both training and validation losses decrease slowly within the range of 0.04–0.07 with slight fluctuations. The model achieves a relatively stable convergence within

approximately 30 epochs, demonstrating good optimisation performance and generalisation capabilities.

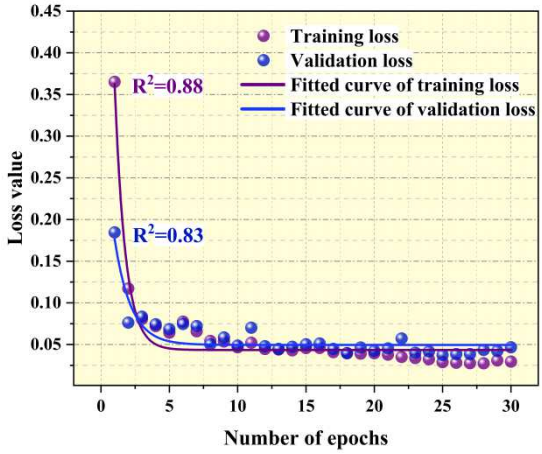


Fig. 4. Loss curves of the ECL model.

In terms of overall performance, the ECL algorithm achieves very high accuracy in P-wave arrival-time picking, as shown in Table 1. In this study, ±0.3 s is used as the accuracy criterion. Among the 6,811 samples in the training set, 99.28% are picked accurately, and the accuracy on the 1,703 validation samples reaches 99.35%, indicating good generalisation capability. The MAE for the training and validation sets are 0.086 s and 0.083 s, respectively, demonstrating stable performance in terms of precision. The model also provides high-accuracy arrival-time estimates on a continuous time scale, offering reliable support for real-time P-wave arrival-time picking under HSR operating conditions.

Table 1. Performance of the ECL Algorithm on the Training and Validation Sets

Split	Accuracy (%)	MAE (s)
Training set	99.28	0.086
Validation set	99.35	0.083

Compared with constructing Conv1D or LSTM models directly on raw waveforms, the ECL joint architecture fully leverages the complementary strengths of

the three components. EMD, as a front-end module, decomposes the strongly non-stationary raw seismic signals into IMFs with clear frequency-band characteristics, effectively reducing the interference of complex noise and trend terms on subsequent feature learning. Conv1D automatically extracts local time–frequency structures from multiple IMFs, replacing traditional handcrafted feature construction. LSTM captures phase evolution and energy accumulation processes at a global time scale, enabling refined localization of the P-wave arrival time.

2.3 *Algorithm Evaluation Metrics*

To meet the stringent requirements of HSR-EEW for the accuracy and stability of P-wave arrival-time picking, this study quantitatively evaluates different picking algorithms from two aspects: time error and engineering applicability. Let the manually picked ground-truth P-wave arrival time be t_P^t, and the algorithm-predicted result be t_P^p; the arrival-time error for a single record is defined as:

$$e = t_P^t - t_P^p \tag{1}$$

The MAE is used to quantify the overall level of time deviation:

$$\mathrm{MAE} = \frac{1}{N}\sum_{i=1}^{N}|e_i| \tag{2}$$

where N is the total number of samples, and e_i is the arrival-time error of the i record. MAE directly reflects the average picking deviation of a model on a continuous time scale and is used to evaluate the overall accuracy of each algorithm.

Considering the engineering requirements of practical HSR-EEW systems, and to avoid operational interruptions and economic losses caused by unnecessary emergency braking, this study defines the acceptable error band for HSR operations

as $|e| \le 0.3\text{s}$. It uses the accuracy A, i.e., the proportion of picks falling within this error band, as the primary evaluation metric:

$$A = \frac{1}{N}\sum_{i=1}^{N} f\left(|e_i| \le 0.3\right) \tag{3}$$

where $f\left(|e_i| \le 0.3\right)$ denotes the hit rate within the ±0.3 s error range.

3. Results and Analysis

3.1 Accuracy Evaluation of the Algorithms

In this study, EMD is used for seismic waveform decomposition and for mitigating non-stationary interference, rather than directly determining the arrival time. Therefore, to quantitatively evaluate the overall performance improvement achieved by the ECL algorithm, it is compared with the STA/LTA, AIC, EC, and EL algorithms. A total of 3,559 P-wave samples were randomly selected from the Japanese K-NET and KiK-net networks for testing, as shown in Fig. 5.

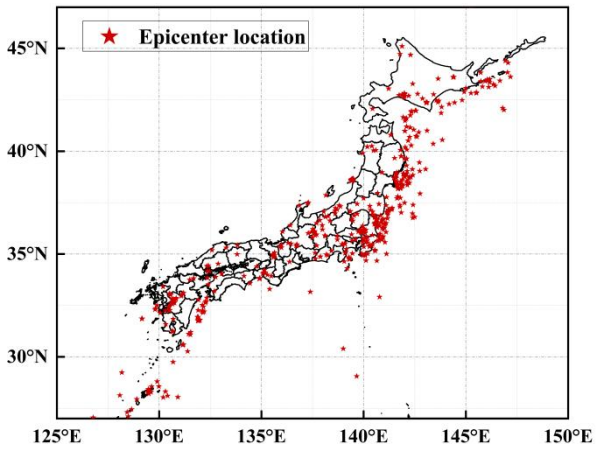


Fig. 5. Distribution of epicenter distance.

The different algorithms show clear differences in P-wave arrival-time picking accuracy and time error, as summarized in Table 2. To verify the effectiveness of each component in the ECL algorithm, the key module structures in the ECL, EC, and EL

algorithms are kept consistent.

Table 2. Performance Comparison of Different Algorithms

Algorithms	Accuracy (%)	MAE (s)
EMD–Conv1D–LSTM	98.6	0.097
EMD–LSTM	80.6	0.274
EMD–Conv1D	69.2	4.442
STA/LTA	77.4	0.698
AIC	85.2	0.608

The ECL algorithm achieves the best overall performance, delivering an accuracy of 98.6% within the ±0.3 s error band and an MAE of only 0.097 s, which meets the engineering requirements of high accuracy and reliability for HSR-EEW. In comparison, EL yields an accuracy of 80.6% with an MAE of 0.274 s, whereas EC achieves an accuracy of only 69.2% and an MAE as high as 4.442 s. These results indicate that although EMD can decompose strongly non-stationary waveforms into multiple IMFs, highlighting the high-frequency transient features associated with the P-wave onset, using Conv1D alone to extract local morphological and energy features is still insufficient for stable arrival-time localisation. Under complex noise conditions, non-seismic interferences such as local spiky pulses and short-term energy jumps are mixed with P-wave-like patterns. By modelling long-range temporal dependencies through gated mechanisms, LSTM can exploit the dynamic evolution before and after the phase onset to suppress local misclassifications and reduce large-error cases. Therefore, Conv1D and LSTM are complementary within the ECL architecture: Conv1D enhances local discriminative capability, while LSTM provides global temporal constraints, and their combination is key to achieving high-precision P-wave

arrival-time picking.

The overall performance of the two conventional methods is relatively limited. STA/LTA achieves an accuracy of 77.4% with an MAE of 0.698 s, while the AIC method attains an accuracy of 85.2% but with an MAE of 0.608 s. In comparison, ECL reduces MAE by approximately 86% and 84% relative to STA/LTA and AIC, respectively, and increases accuracy by approximately 21% and 13%, respectively.

Based on the error samples, cumulative distribution function (CDF) curves of absolute errors were constructed for the five methods. From the perspective of probability distributions, the overall convergence characteristics of the arrival-time errors were compared, as shown in Fig. 6.

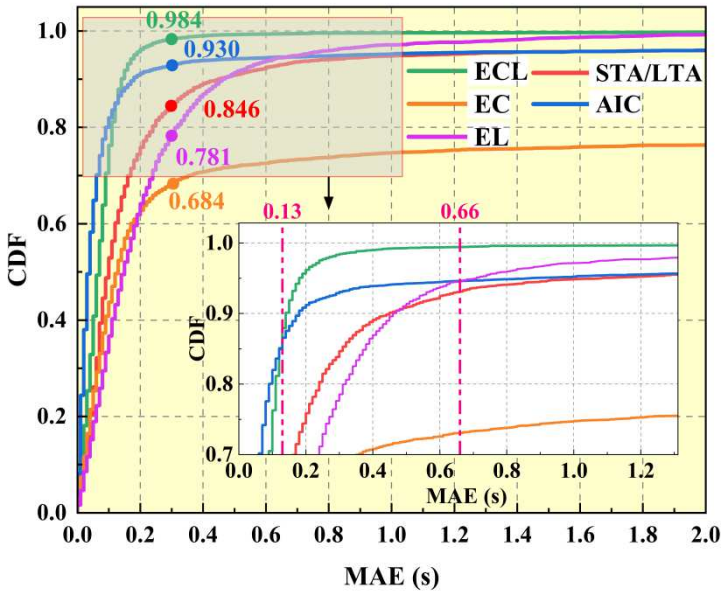


Fig. 6. CDF curves of absolute errors.

When the error threshold is 0.3 s, the CDF values of ECL, AIC, STA/LTA, EL, and EC are 0.984, 0.930, 0.846, 0.781, and 0.681, respectively. These results indicate that under the same time-error constraint, ECL covers the largest proportion of cases, followed by AIC, whereas STA/LTA and EL still have a considerable proportion of

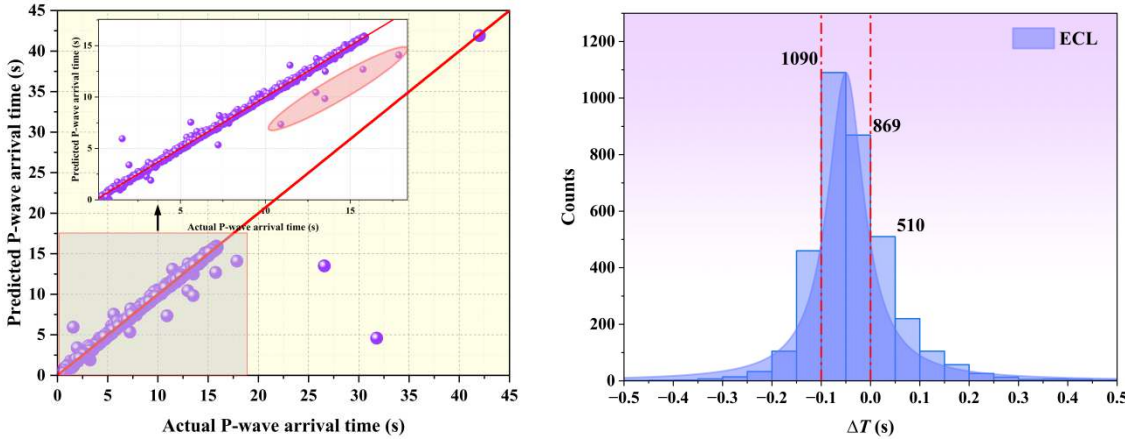
events with errors exceeding 0.3 s, and EC exhibits the most dispersed error distribution. When the error threshold exceeds 0.66 s, the CDF curve of EL surpasses that of AIC; at this stage, the CDF curves of both ECL and EL are already close to 1, indicating that AI-based algorithms show clear advantages in error correction and overall robustness. In contrast, over relatively larger error ranges, the CDF curves of the conventional STA/LTA and AIC methods become flatter, and their picking accuracy is difficult to improve further, indicating evident performance saturation. Overall, ECL performs best across all metrics, with the smallest MAE, a highly concentrated error distribution, and a marked reduction in large-error cases, which better meets the comprehensive requirements of high accuracy, low dispersion, and engineering reliability for HSR earthquake early-warning systems.

3.2 Error Analysis of the Algorithm

The predicted P-wave arrival times of the ECL algorithm show a high level of agreement with the ground truth. Most scatter points are tightly distributed around the ideal reference line $y=x$, with only a small number of samples deviating from this band, as shown in Fig. 7(a). The few large-error points of ECL mainly occur in records with relatively late P-wave arrivals. In these records, long-duration low-frequency noise, weak foreshocks, or surface-wave components may exist prior to the P-wave arrival. After EMD decomposition, some resulting intrinsic mode functions exhibit time–frequency characteristics similar to those of the initial P-wave, leading to slight picking errors.

As shown in Fig. 7(b), the time error ΔT exhibits an approximately unimodal

distribution, with the main peak located at about −0.05 s. Approximately 95% of the samples have errors within the interval of [−0.19,0.17] s, indicating that the ECL algorithm yields a small overall MAE and a highly concentrated error distribution. For the vast majority of events, the picking error is constrained within 0.1 s.



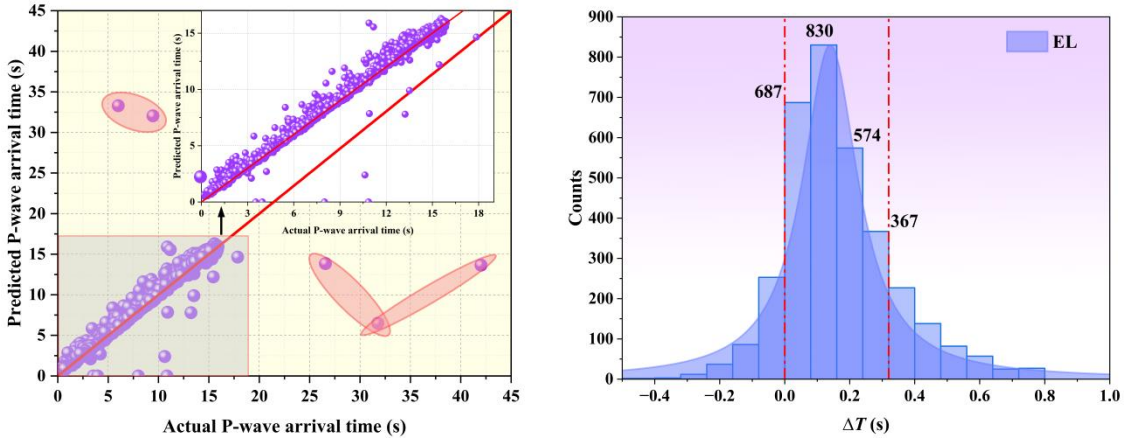
(a)Scatter plot of P-wave arrival times **(b)Histogram of time-error distribution**

Fig. 7. ECL algorithm performance.

The EL algorithm exhibits a markedly higher degree of dispersion than ECL, with larger prediction fluctuations, as shown in Fig. 8(a). As the P-wave arrival time increases, some samples gradually deviate from the banded region and exhibit more pronounced errors, indicating the model's insufficient robustness under far-field, low signal-to-noise ratio, or complex phase conditions.

As shown in Fig. 8(b), the error distribution of EL is broader. The main peak shifts toward the region of $\Delta T>0$, with the peak located at approximately 0.1 s, and most samples have errors concentrated in the range of 0–0.3 s. These results indicate that without incorporating Conv1D, EL relies only on the temporal memory and gating mechanisms of LSTM to model waveform evolution. It is less sensitive to the small-amplitude, extremely short-duration transients at the P-wave onset, and is more

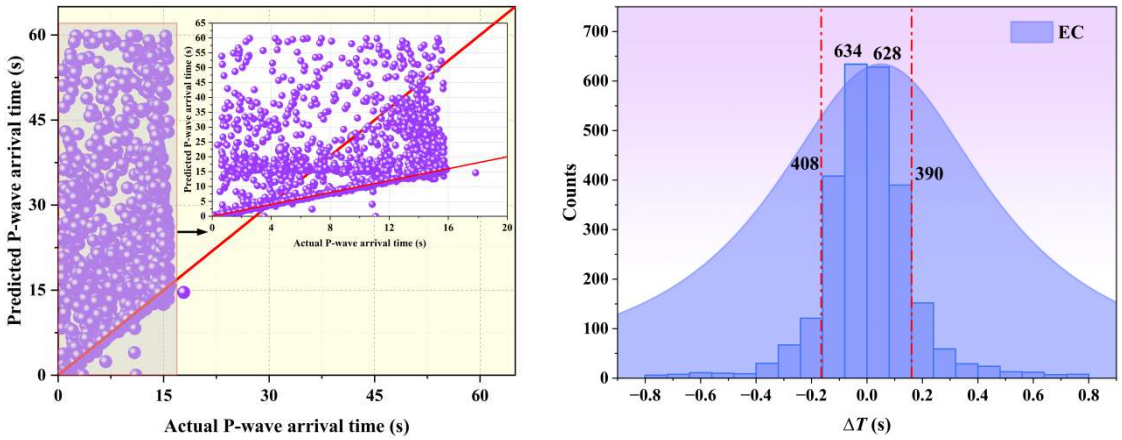
likely to respond to subsequent segments with larger amplitudes and more concentrated energy.



(a)Scatter plot of P-wave arrival times **(b)Histogram of time-error distribution**

Fig. 8. EL algorithm performance.

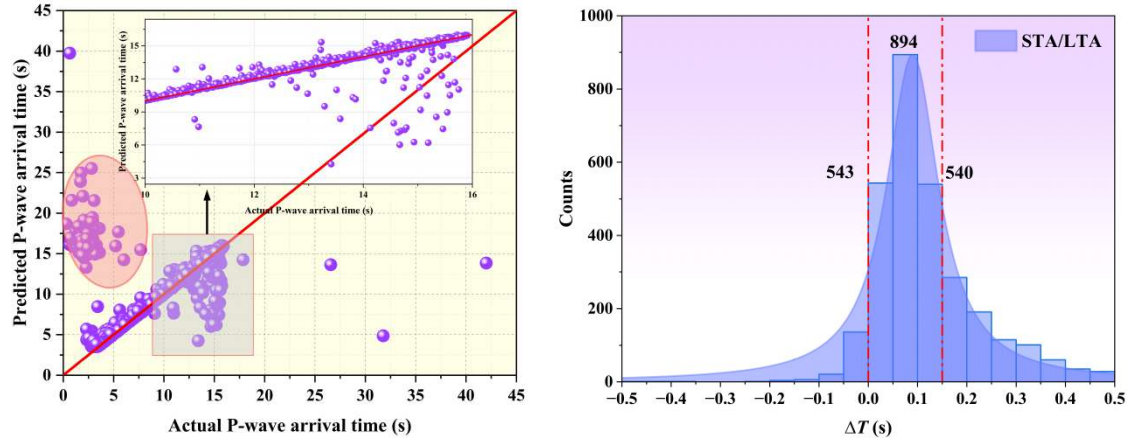
The EC algorithm exhibits poor overall performance, characterised by a high number of erroneous cases and an inability to accurately detect P-wave arrivals, as illustrated in Fig. 9(a). Although most errors of EC are concentrated within a relatively small range, the overall error distribution is broader, as shown in Fig. 9(b). The results indicate that EC tends to misidentify phases with stronger energy, such as S waves or surface waves, as the P-wave arrival, leading to large prediction errors. While this algorithm can extract short-term local morphological features, it lacks global temporal modelling and physically consistent constraints.



(a)Scatter plot of P-wave arrival times **(b)Histogram of time-error distribution**

Fig. 9. EC algorithm performance.

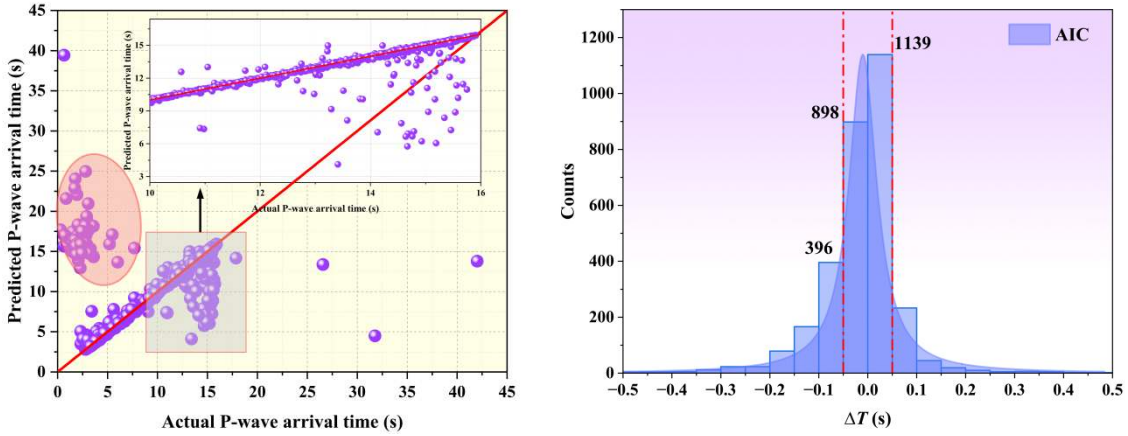
Compared with the ECL and EL algorithms, the STA/LTA method exhibits clustered systematic biases in local regions, indicating poor stability in P-wave picking, as shown in Fig. 10(a). As shown in Fig. 10(b), the main peak lies in the region where $\Delta T>0$, and the overall distribution is skewed toward positive values. The error band is clearly wider than that of the ECL algorithm, and the number of large-error cases is also higher. The STA/LTA method has limited adaptability to changes in P-wave morphology and is therefore difficult to meet the engineering requirements for high accuracy and high reliability.



(a)Scatter plot of P-wave arrival times **(b)Histogram of time-error distribution**

Fig. 10. STA/LTA algorithm performance.

Similar to the STA/LTA method, the AIC method also exhibits clustered systematic biases, as shown in Fig. 11(a). The main peak of ΔT is concentrated within the interval of [−0.05, 0.05] s, and the overall distribution is relatively concentrated, indicating higher overall accuracy than STA/LTA, as shown in Fig. 11(b). However, compared with the ECL algorithm, the AIC picking results show a certain degree of delay, and the number of large-error samples increases markedly.



(a)Scatter plot of P-wave arrival times **(b)Histogram of time-error distribution**

Fig. 11. AIC algorithm performance.

By comparing the error scatter plots and distribution characteristics of the five algorithms, the following conclusions can be drawn. The ECL algorithm achieves the smallest overall MAE, with a highly concentrated error distribution, the highest proportion of small-error samples, and the fewest large-error cases, demonstrating a combined advantage of high accuracy, low dispersion, and low risk. The EC algorithm exhibits large errors and fails to pick P-wave arrivals accurately. After introducing EMD, the EL algorithm can suppress noise interference to some extent; however, due to the lack of Conv1D-based discriminative capability for local waveform details, the error variance increases markedly under complex waveforms and low signal-to-noise

ratio conditions, leading to evident bias. The AIC method outperforms STA/LTA and EL in terms of accuracy, providing relatively accurate picks. However, it exhibits clustered systematic biases, and the number of large-error cases is clearly higher than that of ECL. Overall, ECL outperforms EC, EL, AIC, and STA/LTA in terms of accuracy, stability, and engineering reliability, making it more suitable for the stringent requirements of P-wave arrival-time picking in HSR-EEW systems.

3.3 Sensitivity Analysis of the Algorithms

To further elucidate the mechanisms of error generation for different picking algorithms under complex source and station conditions, this study groups samples with absolute errors greater than 0.3 s into a unified set of large-error events and, based on this, performs sensitivity analyses of relevant earthquake parameters. Three metrics are employed for a comparative evaluation of the five algorithms: Pearson's correlation coefficient, standardised regression coefficients, and random-forest feature importance. Pearson's correlation coefficient reflects the overall linear correlation between a single physical parameter and picking error. The correlation coefficient r_j can be expressed as [27]:

$$r_j = \frac{\sum_{i=1}^{n}(x_{ij} - \bar{x}_j)(e_i - \bar{e})}{\sqrt{\sum_{i=1}^{n}(x_{ij} - \bar{x}_j)^2}} \tag{4}$$

where x_{ij} denotes the *j*-th parameter of the *i*-th sample; $\bar{x}_j$ is the sample mean of x_j, and $\bar{e}$ is the sample mean of the error e_i.

Standardised regression coefficients quantify the influence of a single parameter on the error while accounting for the effects of other parameters. The standardized

411 multiple linear regression model is [28]:

412 $$e_i = \beta_0 + \sum_{j=1}^{p} \beta_j \tilde{x}_{ij} + \varepsilon_i \quad (5)$$

413 where β_0 is the intercept term, β_j is the standardized regression coefficient of the
414 j-th parameter, ε_i is the residual term, and $\tilde{x}_{ij}$ denotes the standardized value of the
415 x_{ij}.

416 Random-forest importance provides a ranked assessment of the overall
417 contributions of influencing factors from the perspectives of nonlinearity and
418 parameter interactions. Suppose the random forest consists of K regression trees
419 $\{T_1,...,T_k\}$. By averaging across the K trees, the raw importance I_j^r of parameter x_j
420 in the entire random forest is obtained. I_j^r is then normalized to yield the final
421 feature-importance index I_j [29]:

422 $$I_j^r = \frac{1}{K} \sum_{k=1}^{K} I_j(T_k) \quad (6)$$

423 $$I_j = \frac{I_j^r}{\sum_{l=1}^{p} I_j^r} \quad (7)$$

424 where j is the feature index, which in this study corresponds to magnitude, depth,
425 distance, duration, and peak acceleration.

426 The sensitivity of the ECL algorithm to each parameter is presented in Table 3.
427 The correlation coefficients of all parameters are small, indicating that the linear
428 relationships are not evident. Although magnitude and focal depth have relatively
429 larger values in the standardised regression coefficients, their weights in the
430 random-forest feature importance are low, suggesting that after considering nonlinear

effects and parameter interactions, their practical impact on the error is limited. Epicentral distance has the highest feature importance, but its value is only 0.488, indicating a limited overall influence on the error. Therefore, conventional physical parameters are not the decisive factors causing ECL picking errors, and ECL exhibits good robustness across different conditions of magnitude, focal depth, and epicentral distance. The errors are more likely to arise from non-physical factors such as local site conditions, differences in station instrument responses, and the distribution of training samples.

Table 3. Sensitivity Analysis of Parameters for the ECL Algorithm

Feature	Mean	Standard Deviation	Correlation Coefficient	Standardized Regression Coefficient	Feature Importance
Duration（s）	90.039	29.557	0.139	-1.083	0.125
Peak acceleration（cm/s²）	9.022	10.360	0.007	-0.956	0.232
Distance（km）	156.915	139.255	0.229	0.450	0.488
Depth (km)	54.392	40.141	0.262	1.145	0.092
Magnitude	5.290	1.107	0.225	1.234	0.063

The sensitivity of the EL algorithm to each parameter is summarised in Table 4. The correlation coefficients between the parameters and the errors are generally small, and the standardised regression coefficients are also low, indicating that the linear relationship between the error and any single physical parameter is not strong. Epicentral distance shows the highest random-forest feature importance, reaching 0.578, suggesting that EL is more sensitive to variations in epicentral distance and is more likely to produce errors when the station-to-epicentre distances vary substantially. Except for epicentral distance, the influences of the other ground-motion parameters on EL errors are limited, and the overall sensitivity remains at a low level.

449 **Table 4. Sensitivity Analysis of Parameters for the EL Algorithm**

Feature	Mean	Standard Deviation	Correlation Coefficient	Standardized Regression Coefficient	Feature Importance
Duration（s）	89.488	29.668	0.016	-0.045	0.195
Peak acceleration（cm/s²）	14.369	18.064	-0.026	-0.005	0.146
Distance（km）	117.695	87.679	0.094	0.222	0.578
Depth (km)	50.877	30.646	0.042	-0.015	0.039
Magnitude	5.263	0.809	0.028	-0.059	0.042

450 The sensitivity of the EC algorithm to each parameter is presented in Table 5.
451 Although the overall error is large, the sensitivities between the parameters and the
452 error are all small. The highest feature importance is observed for epicentral distance,
453 but the value is only 0.489, indicating that source-related parameters have limited
454 overall explanatory power for the error.

455 **Table 5. Sensitivity Analysis of Parameters for the EC Algorithm**

Feature	Mean	Standard Deviation	Correlation Coefficient	Standardized Regression Coefficient	Feature Importance
Duration（s）	82.331	27.473	0.076	-0.079	0.235
Peak acceleration（cm/s²）	13.790	22.785	-0.023	-0.006	0.220
Distance（km）	101.173	77.641	0.180	0.158	0.489
Depth (km)	45.626	28.783	0.109	0.021	0.023
Magnitude	4.948	0.887	0.128	0.067	0.034

456 The parameter sensitivity of the STA/LTA method is summarised in Table 6,
457 where peak acceleration shows the most pronounced influence on the error. The
458 correlation coefficient between peak acceleration and the error reaches 0.568, the
459 standardised regression coefficient is 3.114, and the random-forest feature importance
460 is 0.676, indicating that STA/LTA is highly sensitive to variations in motion amplitude
461 and is prone to large picking deviations under conditions with intense fluctuations. In
462 contrast, the correlation coefficients, regression coefficients, and importance metrics

of the other parameters are all markedly lower, suggesting limited influence on the error.

Table 6. Sensitivity Analysis of Parameters for the STA/LTA Algorithm

Feature	Mean	Standard Deviation	Correlation Coefficient	Standardized Regression Coefficient	Feature Importance
Duration（s）	73.288	23.021	0.152	-0.159	0.075
Peak acceleration（cm/s²）	7.143	10.336	0.568	3.114	0.676
Distance（km）	110.134	66.574	-0.052	0.212	0.175
Depth (km)	45.800	25.982	0.044	-0.343	0.021
Magnitude	4.782	0.797	0.068	-0.426	0.052

The parameter sensitivity results of the AIC method are presented in Table 7. The correlation coefficient between peak acceleration and the error is as high as 0.558, the standardised regression coefficient is 3.607, and the random-forest feature importance is 0.714, indicating that the AIC method is highly sensitive to variations in motion amplitude and is more likely to produce large picking deviations for high-acceleration records. In contrast, the correlation coefficients and feature importances of duration, epicentral distance, focal depth, and magnitude remain at low levels, suggesting limited influence on the error.

Table 7. Sensitivity Analysis of Parameters for the AIC Algorithm

Feature	Mean	Standard Deviation	Correlation Coefficient	Standardized Regression Coefficient	Feature Importance
Duration（s）	72.228	22.052	0.203	0.117	0.048
Peak acceleration（cm/s²）	7.851	12.934	0.558	3.607	0.714
Distance（km）	111.170	59.973	-0.074	0.055	0.172
Depth (km)	47.157	25.432	0.050	-0.292	0.027
Magnitude	4.790	0.799	0.084	-0.506	0.039

Overall, clear differences are observed in the dominant factors controlling errors between AI-based and traditional algorithms. For ECL, EL, and EC, the sensitivities

of all parameters are small, and epicentral distance is the relatively dominant physical factor affecting the picking performance of the deep-learning models. Variations in epicentral distance can change the frequency-band characteristics of the waveforms, thereby influencing the time–frequency feature extraction of EMD and the discrimination of the P-wave onset by the deep network. When the distributions of near-field and far-field samples are imbalanced, deep-learning models are more likely to exhibit a certain degree of systematic bias during training and testing. In contrast, the sensitivity analyses of STA/LTA and AIC indicate that amplitude levels mainly govern their errors. For high-acceleration records, abrupt energy changes can enlarge the short-to-long window energy ratio or alter the shape of the AIC function curve, which can easily lead to premature or delayed triggering. Under low-acceleration and low signal-to-noise ratio conditions, noise segments are more likely to be misidentified as P waves. Overall, AI-based algorithms exhibit better robustness to conventional source parameters, whereas traditional STA/LTA and AIC methods rely heavily on amplitude features, and peak acceleration is the primary factor that amplifies their errors under complex motion conditions.

3.4 First-Station Accuracy Analysis

The first station receives the initial P-wave arrival earliest, and its picking accuracy directly determines the response timeliness and alarm reliability of an EEW system. To evaluate the engineering applicability of different algorithms under the earliest-arriving station condition, this study extracts 972 earliest-arriving station samples of the Japanese K-NET and KiK-net seismic networks. The spatial

distribution of the corresponding station locations is shown in Fig. 12.

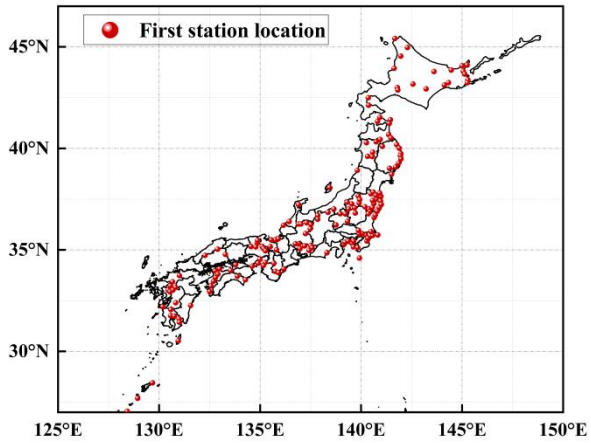


Fig. 12. Spatial distribution of station locations.

The first-arriving station records correspond to the earliest phase-onset interval, imposing more stringent requirements on an algorithm's capability to detect weak initial motion, its noise robustness, and its arrival-time localization accuracy. If the first-station picking achieves high reliability, it can provide prior constraints for subsequent multi-station information fusion and help the EEW system initiate engineering actions earlier. The ECL algorithm performs best on first-station events, achieving 99.1% accuracy with an MAE of only 0.099 s, thereby better supporting the core requirements of rapid response and stable output in HSR-EEW. As shown in Table 8, the accuracies of EL, AIC, STA/LTA, and EC are 92.7%, 90.8%, 82.7%, and 80.0%, with MAEs of 0.386 s, 0.381 s, 0.480 s, and 2.029 s, respectively.

Table 8. Performance at the First-Arriving Station

Algorithms	Accuracy (%)	MAE (s)
EMD–Conv1D–LSTM	99.1	0.099
EMD–LSTM	92.7	0.386
EMD–Conv1D	80.0	2.029
STA/LTA	82.7	0.480

AIC	90.8	0.381

513 **3.5** Robustness Validation under Field-Measured High-Speed Railway Noise

514 This study used field-measured train-passage data collected in 2023 from the
515 Sichuan–Chongqing region by Sichuan Southwest Jiaotong University Railway
516 Development Co., Ltd. to construct a high-speed railway operating-scenario test set.
517 The dataset comprises 147 field records containing mixed train-induced vibration and
518 seismic signals, stored in .UD1 and .UD2 channel formats. Manually picked P-wave
519 arrival times were used as the reference values. To ensure consistency with the
520 original training conditions, the pretrained ECL network architecture and model
521 weights were kept unchanged during testing.

522 Due to space limitations, the field record CYSSATST_20230522035644 was
523 selected as a representative example to further evaluate the P-wave arrival picking
524 performance of the ECL method under high-speed railway operating conditions. This
525 record corresponds to an Ms 4.5 earthquake that occurred at 03:56:44 on May 22,
526 2023, with an epicenter at 28.40°N, 104.83°E and a focal depth of 8 km. The
527 CYSSATST station is located at 29.4072°N, 105.8014°E, with an epicentral distance
528 of approximately 146.6 km. As shown in Fig. 13, the original waveform exhibits clear
529 superposition of train-induced vibration and seismic signals, representing a complex
530 field condition involving sustained vibration, transient disturbances, and seismic
531 P-wave onset.

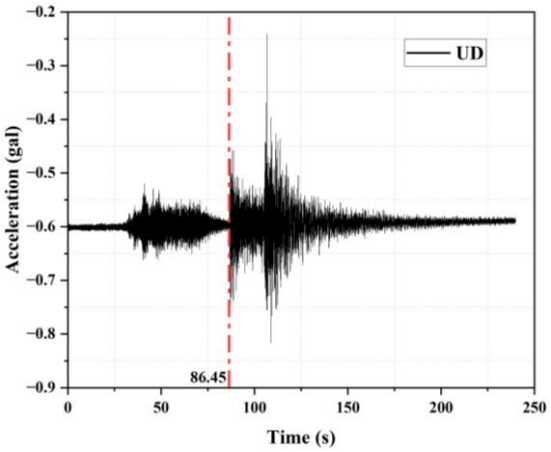


Fig. 13. ECL-Based P-Wave Arrival Picking for Train–Earthquake Mixed Signals.

ECL employs EMD to perform multiscale decomposition of the original nonstationary signal. Using the identified P-wave arrival at 86.45 s as the reference, the IMF components within 2 s before and after the arrival were compared. Before the P-wave arrival, the standard deviations of IMF1, IMF2, and IMF3 were 0.00618, 0.00448, and 0.00085 gal, respectively. Within 2 s after the arrival, they increased to 0.05483, 0.01457, and 0.00566 gal, corresponding to approximately 8.88, 3.25, and 6.69 times their pre-arrival values, respectively, as shown in Fig. 14. These results indicate that EMD decomposition markedly enhances the multiscale feature differences between the pre- and post-P-wave segments.

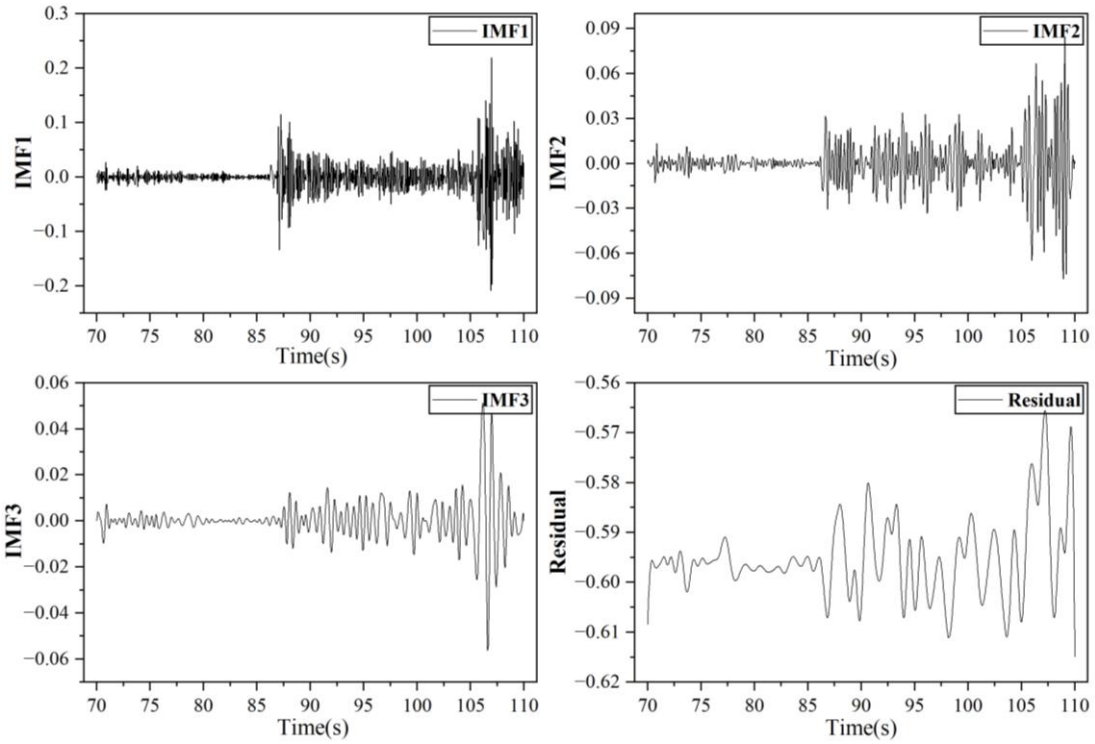


Fig. 14. EMD decomposition results of the train–earthquake mixed signal.

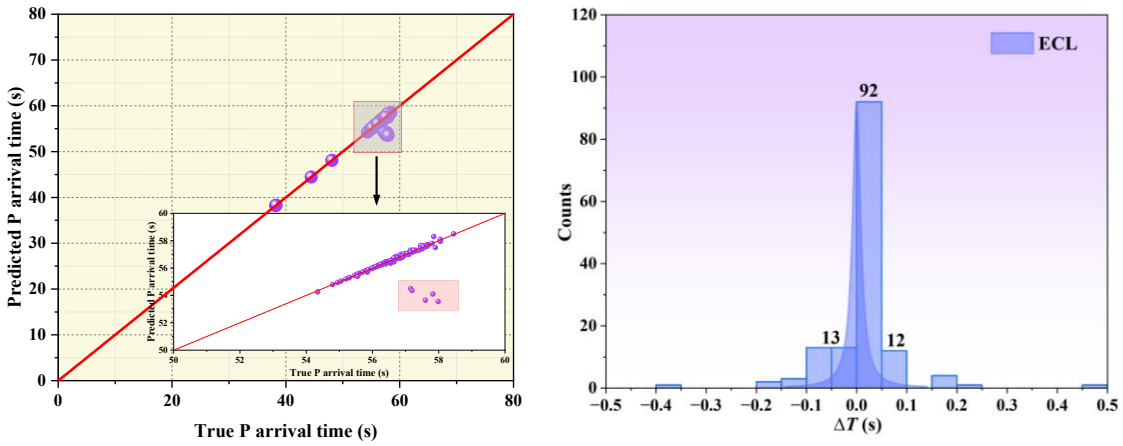
The root-mean-square (RMS) amplitude and peak-to-peak amplitude were analyzed for different time segments, as summarized in Table 9. The signal was divided into the background segment, the train-induced mixed-noise segment, and the intervals before and after the P-wave arrival. In the background segment (approximately 0–20 s), the RMS amplitude was only 0.00240 gal, indicating relatively weak vibration. During the train-induced mixed-noise segment, the RMS increased to 0.01415 gal, approximately 2.92 times that of the pre-P-wave segment, while the peak-to-peak amplitude increased from 0.03457 to 0.14329 gal, indicating substantial vibration interference caused by train operation. Despite the relatively large vibration amplitude in this mixed-noise segment, the ECL method did not trigger prematurely and identified the P-wave arrival at approximately 86.45 s, in close agreement with the manually picked arrival time. These results indicate that

ECL does not rely solely on absolute amplitude for P-wave picking, but instead discriminates train-induced vibration from the true seismic onset through integrated feature representation and temporal modeling. Consequently, the model can still reliably locate the P-wave arrival under train-operation interference.

Table 9. Time-domain characteristics of different signal segments

Signal segment	Time range (s)	RMS (gal)	Peak-to-peak amplitude (gal)	RMS relative to pre-P-wave
Background	0–20	0.00240	0.01645	0.50
Train-induced/mixed-noise segment	25–80	0.01415	0.14329	2.92
Pre-P-wave segment	80–86.45	0.00484	0.03457	1.00
0–2 s after P-wave arrival	86.45–88.45	0.05425	0.28825	11.20
2–8.55 s after P-wave arrival	88.45–95	0.03456	0.28134	7.14

As shown in Fig. 15, for the 147 field-measured train–earthquake mixed records, the ECL method achieved a P-wave arrival picking accuracy of 95.24% and an MAE of 0.155 s. The prediction errors were generally small, with most samples distributed close to the 1:1 reference line and the errors mainly concentrated within ±0.10 s. Only a small number of records showed premature picks. These results demonstrate that ECL maintains high picking accuracy under train–earthquake mixed conditions and exhibits strong robustness to complex operational interference, indicating good potential for practical high-speed railway applications.



(a)Scatter plot of P-wave arrival times **(b)Histogram of time-error distribution**

Fig. 15. P-wave picking and error distribution of ECL for field-measured records.

4. Discussion

The proposed ECL algorithm automatically picks seismic P-wave arrival times. This approach allows mode decomposition to contribute directly to subsequent feature representation and arrival-time determination, thereby enhancing the model's ability to recognize weak onset information and suppress complex background interference. Based on parameter-sensitivity analyses of error samples, this study identifies the dominant factors controlling errors across different algorithms, providing a reliable reference for engineering applications in HSR-EEW systems.

Deep neural network–based phase pickers can reduce the mean error and decrease the number of large-error events across multiple networks and under complex source conditions, but their performance depends to some extent on the training data in terms of magnitude range, source mechanism, and station coverage [30]–[34]. PhaseNet and EQTransformer, as emerging AI-based methods, employ U-Net-like deep convolutional architectures and complex networks integrating CNN, RNN, and

attention mechanisms, respectively, and have achieved high accuracy on large-scale three-component datasets [17,35]. In contrast, the proposed ECL method does not show an increase in network depth or structural complexity. Instead, it is designed to meet the demand for rapid identification of P-wave onset under the complex interference conditions of HSR. In this method, EMD directly participates in subsequent feature representation and arrival-time determination, and, together with a lightweight Conv1D and LSTM architecture, enables high-picking-accuracy arrival-time estimation. The results indicate that, for HSR-EEW, the key to model performance lies not in the network scale itself, but in the degree of alignment among the signal decomposition strategy, the feature representation pathway, and the specific engineering task.

The traditional STA/LTA and AIC methods have simple structures and high computational efficiency and are widely used for phase identification. However, they are highly sensitive to noise, phase superposition, and abrupt amplitude changes. They are prone to trigger shifts and false alarms under complex waveforms and low signal-to-noise ratio conditions [35]–[36]. In contrast, while reducing error levels, the ECL algorithm maintains good performance consistency under different conditions of magnitude, focal depth, and epicentral distance. It can achieve higher engineering reliability without increasing implementation complexity.

Existing studies have mainly investigated how different network modules, loss functions, or feature inputs affect model performance through ablation experiments [34]–[35]. In contrast, quantitative analyses of how ground-motion parameters

609 influence algorithmic accuracy remain relatively limited, and the causes of errors have
610 not been fully explained [16],[39]. Therefore, based on the accuracy evaluation, this
611 study introduces parameter sensitivity analysis to reveal the differences in the
612 dominant factors controlling errors between AI-based and traditional algorithms. The
613 errors of ECL, EL, and EC are relatively sensitive to epicentral distance, whereas
614 STA/LTA and AIC are mainly governed by peak acceleration. When station coverage
615 is uneven or when ultra-long epicentral-distance records are present, deep-learning
616 models may exhibit certain local biases, and their cross-region generalisation
617 capability still needs further verification on larger-scale datasets. Under
618 high-acceleration records, STA/LTA and AIC are more likely to trigger prematurely or
619 with a delay.

620 In seismic phase-identification studies, different algorithms are often evaluated
621 using accuracy metrics based on multi-station information [40]–[42]. By analyzing
622 first-station accuracy, this study is more closely aligned with practical engineering
623 applications of HSR-EEW. Within the shortest warning time window, the EEW
624 pipeline often relies on only a small number of stations for an initial decision;
625 therefore, the reliability of the first-station picking algorithm directly affects the
626 system start time, alarm stability, and the processing speed of subsequent multi-station
627 fusion. First-station accuracy can serve as a key metric that complements
628 conventional average performance evaluation and verifies the practical application
629 value of different algorithms from an engineering reliability perspective.

630 Future work can conduct transfer learning and cross-regional comparative

experiments based on broader regional and network datasets, incorporating environmental features and train-induced noise. In line with the real-time and reliability requirements of HSR-EEW operations, it can systematically evaluate model complexity, computational latency, and deployment cost. This will promote the development of deep-learning-based P-wave picking algorithms toward stable and sustainable engineering applications [43].

5. Conclusions

To meet the engineering requirements of HSR-EEW systems for rapid response, high precision, low false-alarm rate, and low missed-detection rate, this study proposes an automatic P-wave arrival-time picking algorithm that integrates EMD, Conv1D, and LSTM. By comparatively analysing ECL against EL, EC, STA/LTA, and AIC, the performance differences among these algorithms under seismic phase conditions are evaluated in terms of overall accuracy, error distribution characteristics, and parameter sensitivity. The main conclusions are as follows:

(1) The ECL algorithm decomposes strongly non-stationary raw seismic signals into multiple IMFs with different frequency-band characteristics via EMD. Conv1D then extracts multi-channel local morphological and energy-distribution features, and LSTM models the long-range temporal dependencies of seismic signals, enabling accurate estimation of the P-wave arrival time.

(2) In terms of picking accuracy, the ECL algorithm achieves a P-wave arrival-time accuracy of 98.6% with an MAE of only 0.097 s. Compared with the EL, EC, STA/LTA, and AIC algorithms, ECL increases accuracy by 18.0%, 29.4%, 21.2%,

and 13.4%, respectively, and reduces MAE by approximately 0.18 s, 4.35 s, 0.60 s, and 0.51 s, respectively. While substantially reducing time errors, ECL improves phase-identification accuracy and can provide more reliable P-wave arrival-time estimates for HSR engineering applications.

(3) When the error threshold is 0.3 s, the CDF values of ECL, AIC, STA/LTA, EL, and EC are 0.984, 0.930, 0.846, 0.781, and 0.684, respectively. Under the same time constraint, ECL achieves the highest picking accuracy, which better meets the engineering requirements of high precision, low dispersion, and low risk of large errors in HSR-EEW systems.

(4) Traditional methods rely heavily on amplitude features, whereas AI-based algorithms exhibit better robustness to conventional source parameters. The sensitivities of ECL, EL, and EC to conventional ground-motion parameters are low, and their errors are not primarily governed by any single physical variable. Peak acceleration is the dominant factor driving the error amplification of the STA/LTA and AIC methods.

(5) Under the first-station condition, ECL achieves a P-wave picking accuracy of 99.1% with an MAE of 0.099 s. For field-measured train–earthquake mixed records, the accuracy remains as high as 95.24%, with an MAE of 0.155 s, indicating consistently high picking accuracy and stable performance. ECL can provide evidence for practical engineering decision-making and improve the timeliness of responses and the reliability of alarms in HSR-EEW systems.

Authorship Contribution Statement

Xiaoyang Li: Writing – original draft, Methodology, Investigation, Data curation, Conceptualization. **Changwei Yang:** review & editing, Supervision, Funding acquisition. **Jing Lian:** Writing –Funding acquisition, Investigation. **Baorui Hou:** Writing – Data curation , review & editing. **Xinqi Ouyang:** Writing – review & editing, Investigation. **Xinyu Liang:** Investigation, Formal analysis.

Acknowledgments

The authors are grateful for the constructive comments from the editors and anonymous reviewers that significantly improved this work. This research was financially supported by the National Natural Science Foundation of China (Grant Nos. 52502430 and 52372343). In addition, the authors gratefully acknowledge the National Research Institute for Earth Science and Disaster Resilience (NIED) and Sichuan Southwest Jiaotong University Railway Development Co., Ltd. for providing data support.

Disclosure Statement

No potential conflict of interest was reported by the author(s).

Fundinig

This research was financially supported by the National Natural Science Foundation of China (Grant Nos. 52502430, and 52372343).

Data Availability Statement

The data that support the findings of this study are publicly available in the National Research Institute for Earth Science and Disaster Resilience (NIED) K-NET and KiK-net data repository at https://www.kyoshin.bosai.go.jp/en/. This study also used

field-measured train-passage data collected in 2023 from the Sichuan–Chongqing region by Sichuan Southwest Jiaotong University Railway Development Co., Ltd. All data included in this study are available upon request by contact with the corresponding author.

References

[1] Wang, Y., Guo, W., Zeng, C., Huang, R., Yang, S., Nie, Y., ... & Yu, Z. (2024). Shaking table study on high-speed train seismic derailment mechanism and verification of spectrum intensity derailment index. Earthquake Engineering & Structural Dynamics, 53(10), 3287-3317.

[2] Yue, M., Yang, C., Yu, J., Zhang, L., Zhou, S., Su, K., & Ma, H. (2024). Shaking table study on the seismic dynamic behavior of high-speed railway subgrade with pile network composite-reinforced soil. Engineering Geology, 342, 107769.

[3] Lomax, A., Satriano, C., & Vassallo, M. (2012). Automatic picker developments and optimization: FilterPicker—A robust, broadband picker for real-time seismic monitoring and earthquake early warning. Seismological Research Letters, 83(3), 531-540.

[4] Zhang, D., Li, Z., Fu, J., Wang, L., & Wang, J. (2024). IPP: A Seismic P-Wave's Detection Method Based on the Initial Power of the P-Wave. Journal of Earthquake Engineering, 28(3), 603-616.

[5] Allen, R. (1976). Automatic earthquake recognition and timing. In a Workshop on Automatic and Interactive Processing of Network Data, NCER, Menlo Park, Ca.

[6] Baer, M., & Kradolfer, U. (1987). An automatic phase picker for local and

719 teleseismic events. Bulletin of the Seismological Society of America, 77(4),
720 1437-1445.
721 [7] Zhu, X., Chen, B., Wang, X., & Li, T. (2021). Time series segmentation clustering:
722 A new method for S-phase picking in microseismic data. IEEE Geoscience and
723 Remote Sensing Letters, 19, 1-5.
724 [8] Maeda, N. (1985). A method for reading and checking phase times in
725 autoprocessing system of seismic wave data. Zisin, 38, 365-379.
726 [9] Yin, D., Chen, Y., Yang, Y., Cheng, Y., & Zhang, C. (2024). Research on
727 interference signal recognition in p wave pickup and magnitude estimation.
728 Geotechnical and geological engineering, 42(3), 1835-1848.
729 [10] Baillard, C., Crawford, W. C., Ballu, V., Hibert, C., & Mangeney, A. (2014). An
730 automatic kurtosis-based P-and S-phase picker designed for local seismic networks.
731 Bulletin of the Seismological Society of America, 104(1), 394-409.
732 [11] Huang, T. C., & Wu, Y. M. (2019). A Robust Algorithm for Automatic P-wave
733 Arrival-Time Picking Based on the Local Extrema Scalogram. Bulletin of the
734 Seismological Society of America, 109(1), 413-423.
735 [12] Zhu, J., Sun, W., Li, S., Yao, K., & Song, J. (2024). Threshold-based earthquake
736 early warning for high-speed railways using deep learning. Reliability Engineering &
737 System Safety, 250, 110268.
738 [13] Zhang, G., Yang, L., & Jiang, W. (2024). Key technologies of earthquake early
739 warning system for China's high-speed railway. Railway Sciences, 3(2), 239-262.
740 [14] Mousavi, S.M., Ellsworth, W.L., Zhu, W. et al. (2020). Earthquake

741 transformer—an attentive deep-learning model for simultaneous earthquake detection
742 and phase picking. Nat Commun 11, 3952.
743 [15] Ross, Z. E., Meier, M. A., Hauksson, E., & Heaton, T. H. (2018). Generalized
744 seismic phase detection with deep learning. Bulletin of the Seismological Society of
745 America (BSSA), 108(5A), 2894-2901.
746 [16] Mousavi, S. M., Ellsworth, W. L., Zhu, W., Chuang, L. Y., & Beroza, G. C.
747 (2020). Earthquake transformer: an attentive deep-learning model for simultaneous
748 earthquake detection and phase picking. Nature Communications, 11(1), 3952.
749 [17] Zhu, W., & Beroza, G. C. (2019). PhaseNet: A deep-neural-network-based
750 seismic arrival-time picking method. Geophysical Journal International (GJI), 216(1),
751 261-273.
752 [18] Perol, T., Gharbi, M., & Denolle, M. (2018). Convolutional neural network for
753 earthquake detection and location. Science Advances, 4(2), e1700578.
754 [19] Zhu, W., Li, X., Liu, C., Xue, F., & Han, Y. (2019). An STFT-LSTM system for
755 P-wave identification. IEEE Geoscience and Remote Sensing Letters, 17(3), 519-523.
756 [20] Zhu, W., Tai, K. S., Mousavi, S. M., Bailis, P., & Beroza, G. C. (2022). An end-
757 to-end earthquake detection method for joint phase picking and association using deep
758 learning. Journal of Geophysical Research: Solid Earth, 127(3), e2021JB023283.
759 [21] Mousavi, S. M., & Beroza, G. C. (2022). Deep-learning seismology. Science,
760 377(6607), eabm4470.
761 [22] Woollam, J., Rietbrock, A., Bueno, A., & De Angelis, S. (2019). Convolutional
762 neural network for seismic phase classification, performance demonstration over a

763 local seismic network. Seismological Research Letters, 90(2A), 491-502.
764 [23] Flandrin, P., Rilling, G., & Goncalves, P. (2004). Empirical mode decomposition
765 as a filter bank. IEEE signal processing letters, 11(2), 112-114.
766 [24] Tanaka, T., & Mandic, D. P. (2007). Complex empirical mode decomposition.
767 IEEE Signal Processing Letters, 14(2), 101-104.
768 [25] Alzubaidi, L., Zhang, J., Humaidi, A. J., Al-Dujaili, A., Duan, Y., Al-Shamma,
769 O., ... & Farhan, L. (2021). Review of deep learning: concepts, CNN architectures,
770 challenges, applications, future directions. Journal of big Data, 8(1), 53.
771 [26] Yu, Y., Si, X., Hu, C., & Zhang, J. (2019). A review of recurrent neural networks:
772 LSTM cells and network architectures. Neural computation, 31(7), 1235-1270.
773 [27] van den Heuvel, E., & Zhan, Z. (2022). Myths about linear and monotonic
774 associations: Pearson'sr, Spearman's ρ, and Kendall's τ. The American Statistician,
775 76(1), 44-52.
776 [28] Groen, E. A., Bokkers, E. A., Heijungs, R., & de Boer, I. J. (2017). Methods for
777 global sensitivity analysis in life cycle assessment. The International Journal of Life
778 Cycle Assessment, 22(7), 1125-1137.
779 [29] Antoniadis, A., Lambert-Lacroix, S., & Poggi, J. M. (2021). Random forests for
780 global sensitivity analysis: A selective review. Reliability Engineering & System
781 Safety, 206, 107312.
782 [30] Ross, Z. E., Meier, M. A., & Hauksson, E. (2018). P wave arrival picking and
783 first-motion polarity determination with deep learning. Journal of Geophysical
784 Research: Solid Earth, 123(6), 5120-5129.

785 [31] Wang, J., Xiao, Z., Liu, C., Zhao, D., & Yao, Z. (2019). Deep learning for
786 picking seismic arrival times. Journal of Geophysical Research: Solid Earth, 124(7),
787 6612-6624.
788 [32] Zhu, L., Peng, Z., McClellan, J., Li, C., Yao, D., Li, Z., & Fang, L. (2019). Deep
789 learning for seismic phase detection and picking in the aftershock zone of 2008 Mw7.
790 9 Wenchuan Earthquake. Physics of the Earth and Planetary Interiors, 293, 106261.
791 [33] Zhou, Yijian & Yue, Han & Kong, Qingkai & Zhou, Shiyong. (2019). Hybrid
792 Event Detection and Phase-Picking Algorithm Using Convolutional and Recurrent
793 Neural Networks. Seismological Research Letters. 90. 10.1785/0220180319.
794 [34] Zhang, Y., Li, L., Mu, W., Wei, T., Wang, X., & Yu, G. (2025). CNN-KA: A
795 Hybrid P-Phase Picking Method for Microseismic Source Location in Deep Mine
796 With Complex Geological Conditions. IEEE Transactions on Geoscience and Remote
797 Sensing.
798 [35] Jiang, C., Fang, L., Fan, L., & Li, B. (2021). Comparison of the earthquake
799 detection abilities of PhaseNet and EQTransformer with the Yangbi and Maduo
800 earthquakes. Earthquake Science, 34(5), 425-435.
801 [36] Yin, D., Chen, Y., Yang, Y., Cheng, Y., & Zhang, C. (2024). Research on
802 interference signal recognition in p wave pickup and magnitude estimation.
803 Geotechnical and geological engineering, 42(3), 1835-1848.
804 [37] Luo, J., Bespal'Ko, A. A., Lu, D., & Li, B. (2024). Method for the P-wave arrival
805 pickup of rock fracture acoustic emission signals under strong noise. Measurement
806 Science and Technology, 35(8), 086102.

807 [38] Pardo, E., Garfias, C., & Malpica, N. (2019). Seismic phase picking using
808 convolutional networks. IEEE Transactions on Geoscience and Remote
809 Sensing, 57(9), 7086-7092.
810 [39] Li, W., Chakraborty, M., Fenner, D., Faber, J., Zhou, K., Rümpker, G., ... &
811 Srivastava, N. (2022). EPick: Attention-based multi-scale UNet for earthquake
812 detection and seismic phase picking. Frontiers in earth science, 10, 953007.
813 [40] Ross, Z. E., Meier, M. A., & Hauksson, E. (2018). P wave arrival picking and
814 first-motion polarity determination with deep learning. Journal of Geophysical
815 Research: Solid Earth, 123(6), 5120-5129.
816 [41] Tian, J., Tian, Z., Zhang, M., Meng, Q., Zhang, A., Liu, C., & Jia, L. (2024). A
817 novel identification method of microseismic events based on empirical mode
818 decomposition and artificial neural network features. Journal of Applied Geophysics,
819 222, 105329.
820 [42] Chen, K., Li, M., Li, X., Cui, G., Tian, J., Li, J., ... & Zhu, J. (2025). Enhancing
821 Microseismic Event Detection with TransUNet: A Deep Learning Approach for
822 Simultaneous Pickings of P-Wave and S-Wave First Arrivals. Artificial Intelligence in
823 Geosciences, 100129.
824 [43] Berhich, A., Belouadha, F. Z., & Kabbaj, M. I. (2022). A location-dependent
825 earthquake prediction using recurrent neural network algorithms. Soil Dynamics and
826 Earthquake Engineering, 161, 107389.
827 [44] Anikiev, D., Birnie, C., bin Waheed, U., Alkhalifah, T., Gu, C., Verschuur, D. J.,
828 & Eisner, L. (2023). Machine learning in microseismic monitoring. Earth-Science

829 Reviews, 239, 104371.